ISSN 2635-1676, Nanobiotechnology Reports, 2023, Vol. 18, Suppl. 1, pp. S90–S100. © Pleiades Publishing, Ltd., 2023.

NANOMATERIALS FOR FUNCTIONAL AND STRUCTURAL PURPOSES

Effect of the Spark-Plasma-Sintering Temperature on the Structure, Crystallographic Texture, and Thermoelectric Properties of Materials Based on One-Dimensional Particles of $Bi_2Te_{2.7}Se_{0.3}$

M. N. Yapryntsev[a],* and O. N. Ivanov[a]

[a] *Federal State Autonomous Educational Institution of Higher Education "Belgorod National Research University," Belgorod, 308015 Russia*

**e-mail: yaprintsev@bsu.edu.ru*

Received May 4, 2023; revised October 4, 2023; accepted October 4, 2023

Abstract—In this work we obtain and certify one-dimensional particles of the composition $Bi_2Te_{2.7}Se_{0.3}$ of submicron size with an atypical growth direction. Further, the influence of the temperature of spark plasma sintering on the grain morphology and size, crystal-lattice parameters, elemental composition, and density of the samples obtained are investigated. The features of the formation of the crystallographic texture depending on the sintering temperature are also established. A temperature is revealed that allows for preservation of the crystal structure characteristic of the initial powder and materials with an atypical crystallographic texture to obtained. The thermoelectric properties of the materials obtained are also studied.

DOI: 10.1134/S2635167623600992

INTRODUCTION

The technology of the thermoelectric conversion of thermal energy into electrical energy opens up a promising path to environmentally friendly electricity generation through the collection of waste industrial heat [1]. The efficiency of thermoelectric materials is characterized by the dimensionless thermoelectric figure of merit $ZT = S^2T/\rho\kappa$, where S is the Seebeck coefficient, ρ is the electrical resistivity, T is the temperature, and κ is the total thermal conductivity, which is mainly determined by the electronic (κ_e, $\kappa_e = L\sigma T$, L is the Lorentz coefficient) and lattice (κ_p) contributions [2–7]. The electrical resistivity is determined by both the concentration (n) and mobility (μ) of charge carriers [8–10]. A major challenge in creating high-performance thermoelectric materials is the strong relationship between the electrical and thermal transport properties. One of the promising modern concepts for resolution of the thermoelectric properties is the concept of the 3D transport of charge carriers and 2D transport of phonons [1, 11–16].

Materials based on bismuth telluride are the most common commercial low-temperature thermoelectric materials. The crystal structure of Bi_2Te_3 is a rhombohedral type of tetradymite with the $R\bar{3}m$ space group and is described by a hexagonal unit cell. The unit cell consists of five covalently bonded monoatomic sheets along the c axis in the sequence

$$-Te_{(1)}-Bi-Te_{(2)}-Bi-Te_{(1)}- .$$

Here (1) and (2) denote two different chemical states of tellurium. The nature of the bond between adjacent layers $Te_{(1)}$ is the weak van der Waals interaction, while the bond between bismuth and tellurium atoms is covalent with a small ionic contribution. Because of this crystal structure, the lattice parameter c (3.045 nm) is approximately 7 times larger than a, b (0.438 nm), resulting in a striking anisotropy [17–20]. Significant progress in increasing ZT has been achieved through the specific structuring of bulk materials obtained from nanoscale powders by consolidating them using spark plasma sintering (SPS) while maintaining the morphology and crystallographic orientation of the particles of the initial powder [21]. Chemical methods of synthesis in a solution make it possible to effectively control the morphology, crystal structure, and direction of growth of synthesized particles based on bismuth chalcogenides [22]. Thanks to extensive efforts aimed at developing methods for the controlled synthesis of nanostructures to improve their thermoelectric figure of merit, nanostructures based on Bi_2Te_3 such as nanoplates [23–28], ultrathin nanostructures [29, 30], nanoscale heterostructures [31–34] and one-dimensional nanoparticles [35–37] have been obtained. In particular, it was theoretically predicted [38] and experimentally confirmed [39] that the use of one-dimensional nanostructures, such as nanowires, can help to improve power factor ($S^2\sigma$) due to the quantum confinement effect [38] and to achieve low level of κ_p due to phonon scattering on the surface of nanostructures [39].

However, the lattice structure features of bismuth-telluride-based materials in combination with uniaxial densification techniques usually result in the formation of a crystallographic texture. As a rule, the texturing axis (0 0 1) coincides with the direction of SPS pressing. The features of texturing of materials based on Bi_2Te_3 are described in detail in [40–47]. It is shown that the formation of a quasi-two-dimensional structure is determined by the morphology of particles in the initial powders, the direction of their growth, and recrystallization processes during compaction. However, the low electrical resistance of such polycrystalline materials has been discredited by relatively high thermal conductivity [46, 47]. Therefore, it is necessary to develop methods for optimizing the compaction of bulk polycrystalline materials based on one-dimensional nanostructures with well-controlled composition, morphology and crystallographic orientation, high density, low thermal conductivity, and high electrical conductivity.

On the one hand, there is the possibility of obtaining one-dimensional particles and the prospect of creating bulk materials based on them by rapid compaction using the SPS method; and on the other hand, due to the structural features of the crystal lattice, the recrystallization process leads to destruction of the structure of the rods with the formation of highly textured materials (the texturing axis (0 0 l) coincides with the direction of SPS pressing). This prevents implementation of the benefits of materials based on one-dimensional particles.

MATERIALS AND METHODS

Analytically pure chemical reagents were used without additional purification. In a typical preparation procedure, the required amount (0.125 mol) of sodium hydroxide (NaOH) was dissolved in 200 mL of 1,2-ethanediol under continuous heating and magnetic stirring to form a clear solution. At temperatures of 100–110°C, 0.108 mol of tellurium oxide (TeO_2) and 0.012 mol of selenium oxide (SeO_2) were added to the resulting solution. After their complete dissolution, the volume of the reaction medium was adjusted to 1 L with 1,2-ethanediol and heated to 180°C, kept at this temperature for 2 h, and naturally cooled to 140°C. Then 0.04 mol of bismuth oxide (Bi_2O_3), and an additional 0.125 mol of NaOH and 500 mL of ethylene glycol were added. After this, the reaction medium was heated to 180°C and kept isothermally for 4 h. The resulting precipitate was separated by centrifugation, washed several times with propan-2-ol to pH 7 and then with 2-propanone to remove impurities. The resulting powders were dried at room temperature for 8 h.

To obtain bulk samples, the initial powders based on $Bi_2Te_{2.7}Se_{0.3}$ rods were subjected to the SPS process using the SPS 25/10 system (Thermal Technology, LLC, USA). The synthesized powder materials were sintered in a graphite mold with an internal diameter of 20 mm at a vacuum level of 1.5 Pa, pressure of 40 MPa, and various temperatures (T_s = 530, 580, 630, and 680 K) for 15 min.

A JEM-2100 transmission electron microscope (TEM) (JEOL) was used to characterize the size, morphology, and crystallographic growth direction of particles in the initial powder. To determine the phase composition and crystal-lattice parameters of the powder materials and bulk samples, X-ray phase analysis (XPA) was performed using a SmartLab diffractometer (Rigaku) with CuK_α radiation. Scanning electron microscopy (SEM) was used with a Quanta 600 scanning electron microscope (FEI) to study the particle morphology, estimate the average particle size of the initial powder material, and study the grain structure features of the bulk materials. The bulk samples were also examined by electron backscatter diffraction (EBSD). The sample surface was prepared by vibration polishing. To perform EBSD analysis, the TSL, OIM system (Velocity EBSD camera) was used [48]. Energy dispersive X-ray spectroscopy (EDX) using an Octane Elite EDS system (EDAX AMETEK, Inc.) was used to determine the chemical composition of the initial powder and bulk bismuth–telluride materials. The characteristic lines Bi–L, Te–L, and Se–K were used to calculate the elemental composition.

To study the transport properties of bulk samples, rods 2 × 2 × 10 mm and disks ∅10 × 2 mm were prepared. A ZEM-3 system (ULVAC Advance-Riko) was used to measure the electrical resistivity and Seebeck coefficient of the rods using the four-probe method. Thermal-constant measurement system TC-1200RH (ULVAC Advance-Riko) was used to measure the total thermal conductivity of the disc-shaped samples by laser flash in vacuum. The dependences $\rho(T)$, $S(T)$, and $k_t(T)$ were taken for temperatures from 290 to 520 K. Taking into account the accuracy of the systems and the accuracy of measurements, an error of 5% was estimated when measuring the Seebeck coefficient; 1%, when measuring the electrical resistivity; and 5%, when measuring the thermal conductivity.

RESULTS AND DISCUSSION

Although bismuth-telluride-based materials are characterized by the formation of a crystallographic texture, where the texture axis (0 0 l) coincides with the SPS pressing direction, control of the crystallographic texture can potentially contribute to partial resolution of the thermoelectric properties (ρ, S, k) due to the formation of an atypical crystallographic texture.

In an attempt to study the applicability of crystallographic-texture inversion as a way to optimize the thermoelectric properties, anisotropic 1D particles with an atypical crystallite growth direction (along the

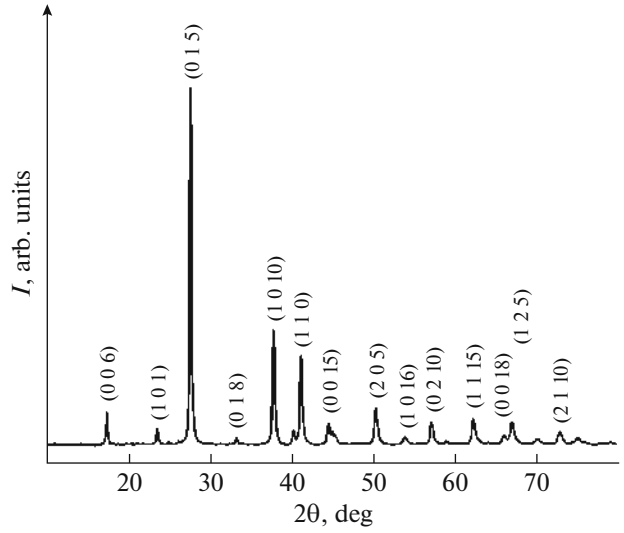

Fig. 1. X-ray diffraction pattern of the initial powder of the composition $Bi_2Te_{2.7}Se_{0.3}$.

crystalline *c* axis) have been obtained. The further strategy of this study was aimed at studying the possibility of maintaining the atypical structure during the transition from a 1D powder material to a bulk one. For this reason, *n*-type thermoelectric material $Bi_2Te_{2.7}Se_{0.3}$, which has been well studied, was chosen as the object of study [49–51]. In order to suppress the recrystallization process, it must be carried out at the optimum temperature in the shortest possible time, so the SPS method was chosen for densification and the initial sintering temperature (T_S) was selected at 680 K as it is optimal for compacting materials of the $Bi_2Te_{2.7}Se_{0.3}$ composition using the SPS method [40–47]. Further, varying the sintering temperature was aimed at determining a T_S value that would allow one to obtain an atypical crystallographic texture and to study the influence of this type of crystallographic texture on the thermoelectric properties.

According to the XPA results, the initial 1D powder was single phase with the crystal-lattice parameters a = 4.383 Å and c = 30.494 Å, which are in good agreement with the standard data for materials based on Bi_2Te_3 (PDF no. 01-089-2009). The X-ray diffraction pattern for the original 1D powder is shown in Fig. 1.

The morphology and sizes of the particles were studied by SEM (Fig. 2a) on a carbon substrate. The SEM image shows that a large number of rods are randomly distributed on the surface of the substrate. Using SEM image analysis, particle-size-distribution histograms were constructed to estimate the average diameter (d_a) and length (l_a) of particles in the initial powder. All histograms were described by a lognormal unimodal distribution. For the $Bi_2Te_{2.7}Se_{0.3}$ d_a = 0.27 μm and l_a = 1.17 μm.

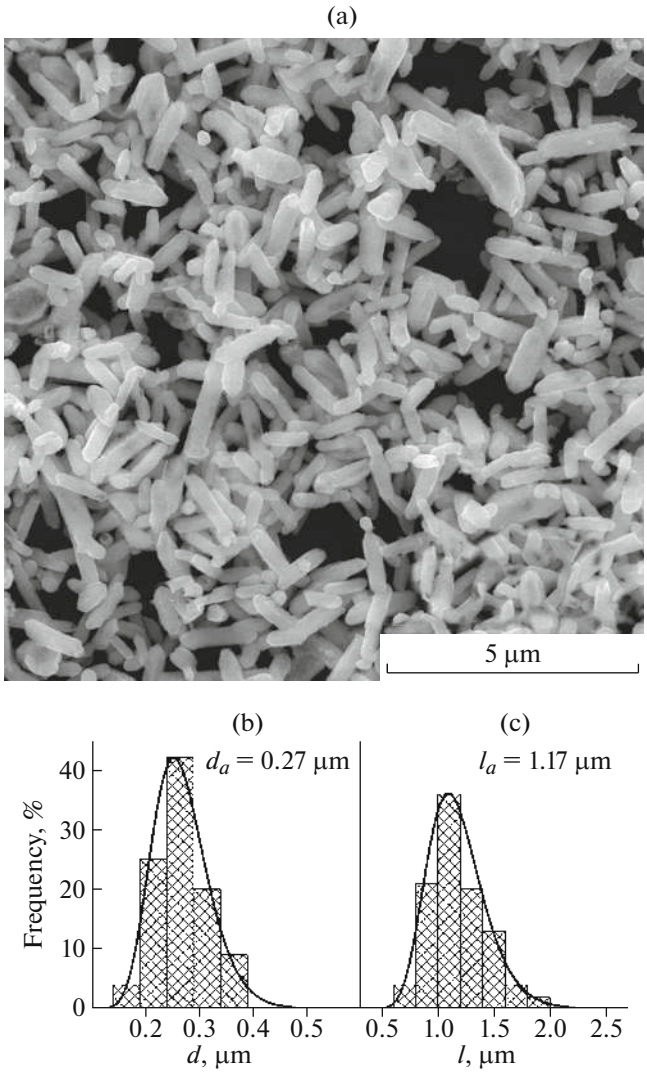

Fig. 2. SEM image (a), histograms of the distribution of the average diameter (b), and average length (c) of the particles of the initial powder material.

Figure 3 shows the TEM images and electron diffraction of a selected region for the $Bi_2Te_{2.7}Se_{0.3}$ sample. Diffraction was carried out in the area marked by a circle (Fig. 3a). The point diffraction pattern was indexed as $Bi_2Te_{2.7}Se_{0.3}$, which is consistent with the XPA results. Next, the diffraction pattern was indexed as a pure $Bi_2Te_{2.7}Se_{0.3}$ phase with the calculated lattice parameters a = 4.384 Å and c = 30.493 Å, the values of which correspond to published data (PDF no. 01-089-2009). The diffraction pattern indicates that crystallites grow along the *c* axis (direction [0 0 1]).

These results indicate that one-dimensional $Bi_2Te_{2.7}Se_{0.3}$ particles were obtained at the synthesis stage. The morphology and growth direction of the synthesized particles are atypical for this class of materials, which should facilitate the production of bulk

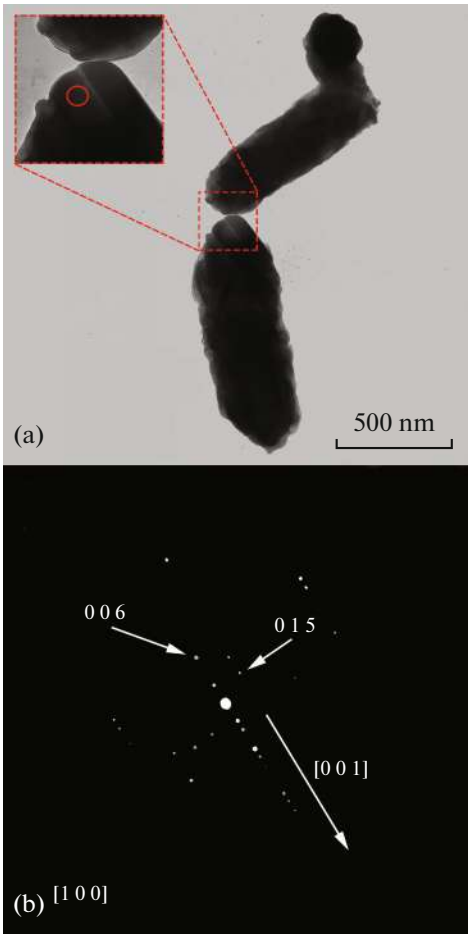

Fig. 3. TEM image (a) and SAED diffraction pattern (b) of the particles of the initial powder material.

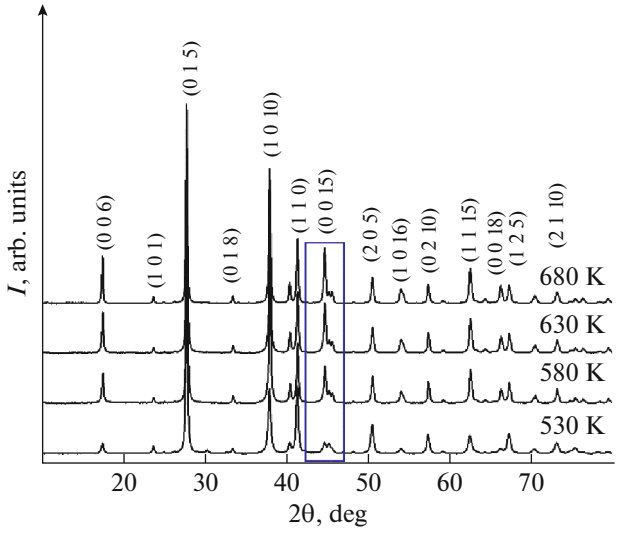

Fig. 4. X-ray diffraction patterns for bulk samples of $Bi_2Te_{2.7}Se_{0.3}$ based on 1D particles, obtained on the surfaces oriented perpendicular to the direction of SPS pressing, sintered at different temperatures (680, 630, 580, and 530 K).

materials with an atypical microstructure and crystallographic orientation.

The synthesized $Bi_2Te_{2.7}Se_{0.3}$ powder based on 1D particles was compacted by SPS. The density of the resulting materials was determined using the Archimedes method. The density naturally increases with increasing temperature (Table 1). X-ray analysis of the bulk samples, carried out on a plane perpendicular to the pressing axis, showed that the consolidated material the is single phase (no reflections corresponding to extraneous phases were detected). As in the case of the powdery material, bulk materials were single phase with a rhombohedral crystal lattice ($R\bar{3}m$ space group), and the calculated lattice parameters decreased with increasing sintering temperature (Table 1).

The X-ray diffraction patterns for the bulk samples are shown in Fig. 4.

The X-ray diffraction patterns presented in Fig. 1 correspond to powdery material with a completely random orientation of 1D particles. If the bulk material obtained from the initial powder consists of randomly located grains, then the X-ray diffraction patterns for the powder and bulk materials will have an identical distribution of intensities of the corresponding reflections. However, upon compaction using the SPS method, the grains must be ordered in a certain plane due to the application of pressure and the recrystallization process. As a result, there will be a preferential orientation of the crystal planes that reflect X-ray radiation. In turn, diffraction patterns

Table 1. Crystal-lattice parameters, grain size, density, and composition (relative to Bi = 2) of bulk $Bi_2Te_{2.7}Se_{0.3}$ samples based on 1D particles obtained by SPS at different temperatures (T_S)

T_S, K	$a = b$, Å	c, Å	D, μm	d, g cm^{-3}	Concentration, at %	
					Te	Se
530	4.358	30.314	0.34	6.76	53.9	5.7
580	4.356	30.283	0.65	6.81	53.8	5.7
630	4.354	30.302	0.87	7.00	53.7	5.7
680	4.352	30.301	1.23	7.34	53.5	5.7

obtained on the surfaces oriented parallel or perpendicular to the axes of pressure application can be different. This difference is associated with redistribution of the intensities of some reflections. This type of redistribution was observed in bulk $Bi_2Te_{2.7}Se_{0.3}$ samples based on 1D particles obtained by SPS at different temperatures (T_S). The redistribution is visible when considering the intensity of reflections (0 0 l). For example, in Fig. 4, the reflections (0 0 15) are highlighted with a rectangle. It can be seen that for T_S = 680, 630, and 580 K, the intensity of reflections (0 0 l) is increased compared to a randomly oriented powder material (Fig. 1). Whereas for a sample sintered at a temperature of 530 K, suppression of the peak intensity (0 0 l) is observed in comparison with the randomly oriented powdery material (Fig. 1). This may indicate inversion of the crystallographic-texture axis. For T_S = 680, 630, and 580 K, it was found that the texture axis is oriented along the crystallographic direction 0 0 1 and parallel to the direction of SPS pressing. There is a noticeable decrease in the relative intensity of reflections (0 0 l) with decreasing sintering temperature, which indicates a decrease in the degree of texturing.

The degree of preferential grain orientation for the samples sintered at T_S = 680, 630, and 580 K can be estimated from the orientation coefficient LF, given by the formula [52]

$$\mathrm{LF} = \frac{p - p_0}{1 - p_0}, \quad (1)$$

where p and p_0 are defined as

$$p = \frac{I(00l)}{\sum I(hkl)}; \quad p_0 = \frac{I_0(00l)}{\sum I_0(hkl)}, \quad (2)$$

where h, k, and l are Miller indices of the corresponding reflection planes.

Here, the intensities I and I_0 correspond to textured and nontextured samples, respectively. Ideally, LF = 1 for a fully oriented sample and LF = 0 for a completely nonoriented sample. The results of calculating the Lotgering coefficient for the samples are LF_{680} = 0.13, LF_{630} = 0.07, and LF_{580} = 0.05. The data obtained confirm the assumption that the degree of texturing increases with increasing sintering temperature. Considering that in all experiments, the same initial powdery material $Bi_2Te_{2.7}Se_{0.3}$ based on 1D particles was used and the compaction parameters, except for temperature, were similar, it can be argued that the formation of the crystallographic texture and its development are a consequence of the recrystallization process. It is important to note that the calculated LF values are small compared to similar data obtained for materials based on 2D particles [53].

SEM images show features of the grain structure of $Bi_2Te_{2.7}Se_{0.3}$ samples based on 1D particles obtained on cleavage surfaces perpendicular and parallel to the direction of pressing of SPS, sintered at different temperatures (Fig. 5).

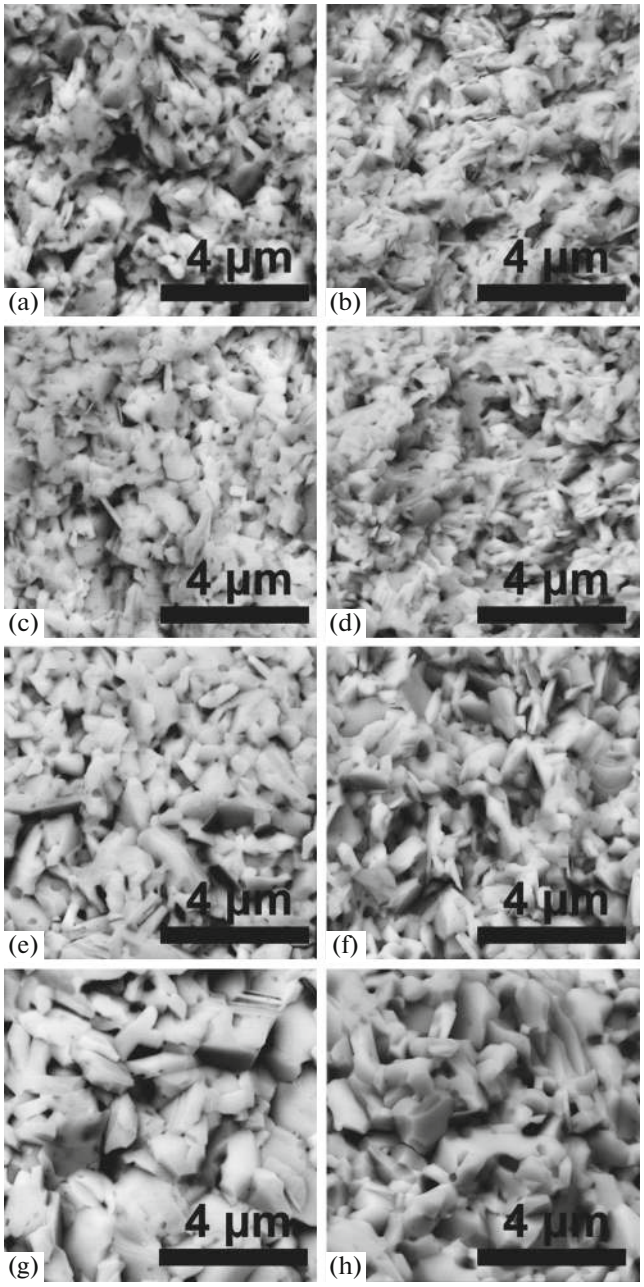

Fig. 5. SEM images for bulk samples of $Bi_2Te_{2.7}Se_{0.3}$ based on 1D particles obtained on the surfaces of chips oriented perpendicular (a, c, e, g) and parallel (b, d, f, h) to the direction of SPS pressing, sintered at temperatures of 680 (a, b), 630 (c, d), 580 (e, f), and 530 (g, h).

As the sintering temperature decreases, the microstructure of the samples changes significantly. A decrease in the sintering temperature leads to a natural decrease in the grain size and density of the resulting materials (Table 1). Regardless of the sintering temperature and direction, the grains have an irregular

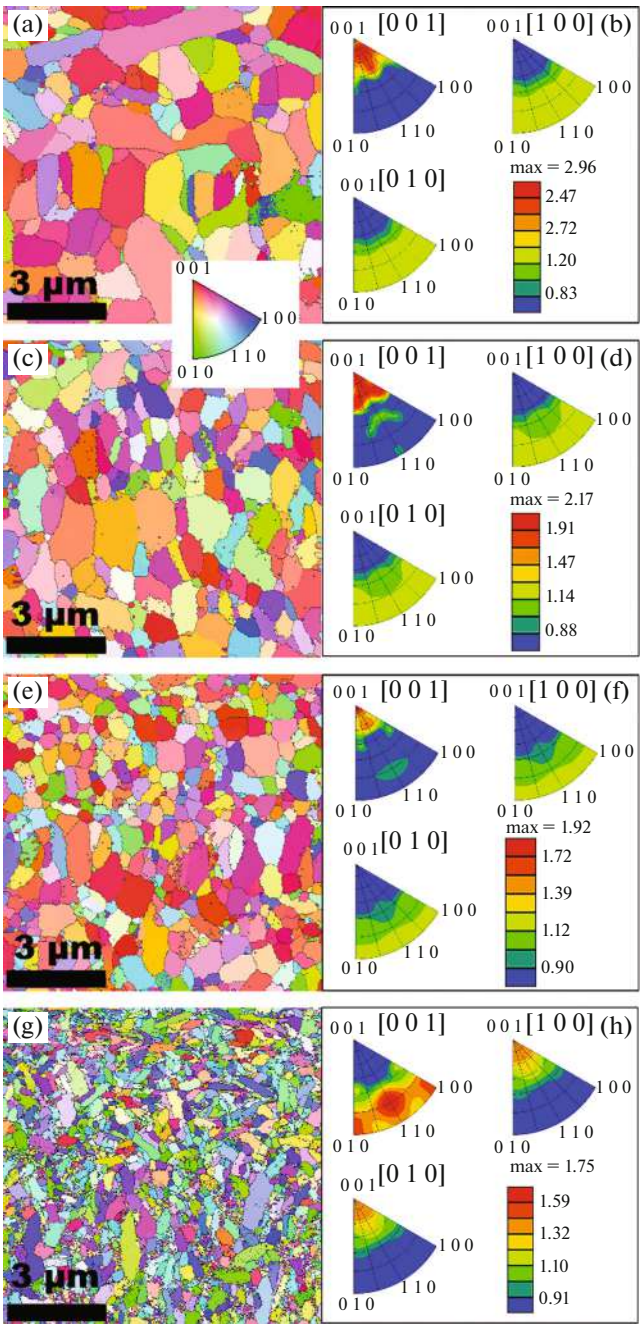

Fig. 6. Orientation distribution maps for bulk samples obtained on surfaces oriented perpendicular to the direction of SPS pressing, sintered at temperatures of 680 (a), 630 (c), 580 (e), and 530 K (g); corresponding inverse pole figures, for samples sintered at 680 (b), 630 (d), 580 (f), and 530 K (h). The inset shows a standard stereographic triangle with color-coded crystallographic directions.

shape. No pronounced anisotropy of the grain structure was detected.

To correctly study the orientation of grains in weakly textured samples, crystallographic orientation distribution (EBSD) maps were constructed. EBSD maps were obtained on highly polished surfaces oriented perpendicular to the direction of SPS pressing (Fig. 6). These maps show the distribution of crystallographic orientations of surface grains. The color of an individual grain is directly related to its crystallographic orientation (inset in Fig. 6).

It can be seen that the samples sintered at temperatures of 680, 630, and 580 K are textured, and the texturing axis is parallel to the direction of SPS pressing, i.e., coincides with the crystallographic axis of three orders. A different type of preferred orientation is observed in the sample sintered at temperatures of 530 K. The initial grains in the form of rods are highly anisotropic with a grain shape factor of $l_a/d_a \approx 4.3$. The particles grow in a certain crystallographic direction, and the recrystallization process is suppressed due to the relatively low temperature, so the crystallographic texture in the bulk material is determined by the packing process of the initial powder particles in the SPS process. Strongly anisotropic grains in the form of rods lie in the plane perpendicular to the pressing axis, i.e., there is some ordering of the grains. On the other hand, the grains lying in this plane are randomly oriented, i.e., the angle between adjacent grains in the form of rods changes randomly. In addition, each grain rotates around its long axis at a random angle. As a result, the crystal axes *a* and *b* of different grains are randomly oriented. However, the crystallographic *c* axis is preferably oriented along the plane perpendicular to the pressing axis. The ordering of these grains may be the reason for weak texturing of the samples sintered at a temperature of 530 K. The formation of a crystallographic texture of this type is due to the influence of uniaxial compression during the SPS process (packing of 1D particles of the initial powder) and suppression of the recrystallization process due to a decrease in the sintering temperature. The change in the primary grain color in the EBSD images obtained for the samples sintered at different temperatures is consistent with the change in texturing discussed above. To confirm the inversion of the crystallographic-texture axis, inverse pole figures were constructed (Fig. 6). It is shown that the samples obtained at T_S = 680, 630, and 580 K are characterized by a crystallographic texture with the (0 0 l) axis parallel to the pressing axis. It is important to note that as the sintering temperature decreases, the sharpness of the texture decreases with a simultaneous reduction in the grain size, which correlates well with the XPA (Fig. 4) and SEM data (Fig. 5, Table 1). For the sample obtained at T_S = 530 K, inversion of the crystallographic-texture axis is observed, as a result of which a biaxial texture (0 1 0) and (1 0 0) is formed, which coincides with the pressing direction.

All thermoelectric properties (ρ, *S*, and *k*) for bulk $Bi_2Te_{2.7}Se_{0.3}$ samples based on 1D particles obtained by SPS at different temperatures were measured for the orientations perpendicular and parallel to the pressing axis. It is known that the transport properties

ρ and k for textured materials based on Bi_2Te_3 largely depend on the direction of measurements [45, 46, 54–59].

The specific electrical resistances measured in directions perpendicular ($\rho_\perp$) and parallel ($\rho_\parallel$) to the pressing axis, differ significantly for the samples obtained at the same temperature, which confirms the anisotropy of the thermoelectric properties. In this case, the anisotropy of the electrical resistivity ($A_\rho = \rho_\parallel/\rho_\perp$) decreases with decreasing SPS temperature ($A_\rho^{680} = 3.1$, $A_\rho^{630} = 1.4$, $A_\rho^{580} = 1.2$; the superscripts correspond to the sintering temperature). The electrical resistivity of a semiconductor is expressed as [60]:

$$\rho = \frac{1}{e\mu_e n}, \quad (3)$$

where e, n, and μ_e are the elementary charge, and the electron concentration and mobility, respectively.

A decrease in the sintering temperature leads to an increase in the electrical resistivity, which is caused by a change in the concentration of charge carriers (n) and their mobility (μ). The concentration and mobility, in turn, are determined by changes in the grain size, density, crystallographic texture, and defect concentration. If the change in the charge-carrier mobility correlates well with the SEM data, then the change in the charge-carrier concentration may be associated with the formation of point defects as a result of tellurium evaporation during the SPS process. Table 1 shows these relationships between the tellurium concentration and sintering temperature.

It is known that the presence and concentration of point defects in materials based on bismuth telluride determines the type and concentration of majority charge carriers [60–64]. The evaporation of tellurium during annealing of the materials based on Bi_2Te_3 occurs due to the anomalously high pressure of saturated tellurium vapors [65–68], the evaporation energy of Te (52.55 kJ/mol) is significantly lower than that of Bi (104.80 kJ/mol) [60]. Deviations from stoichiometry towards a tellurium deficiency naturally lead to the formation of tellurium vacancies and, as a consequence, the formation of two electrons per defect.

Next, the influence of the sintering temperature on the temperature dependences of the Seebeck coefficient was studied. The sign of the Seebeck coefficient is negative, which is consistent with the electronic conductivity of the samples under study. Regardless of the sintering temperature, the Seebeck coefficient is isotropic ($A_S = S_\parallel/S_\perp \approx 1$), which is consistent with theoretical data [69]. An increase in the sintering temperature leads to a decrease in the modulus of the Seebeck coefficient, which is generally consistent with a change in the concentration of the main charge carriers due to the evaporation of tellurium during sintering. All dependences $S(T)$ in Fig. 7b have an extremum, which is also associated with the bipolar effect. It is known [70] that the Seebeck coefficient of a degenerate semiconductor can be expressed as

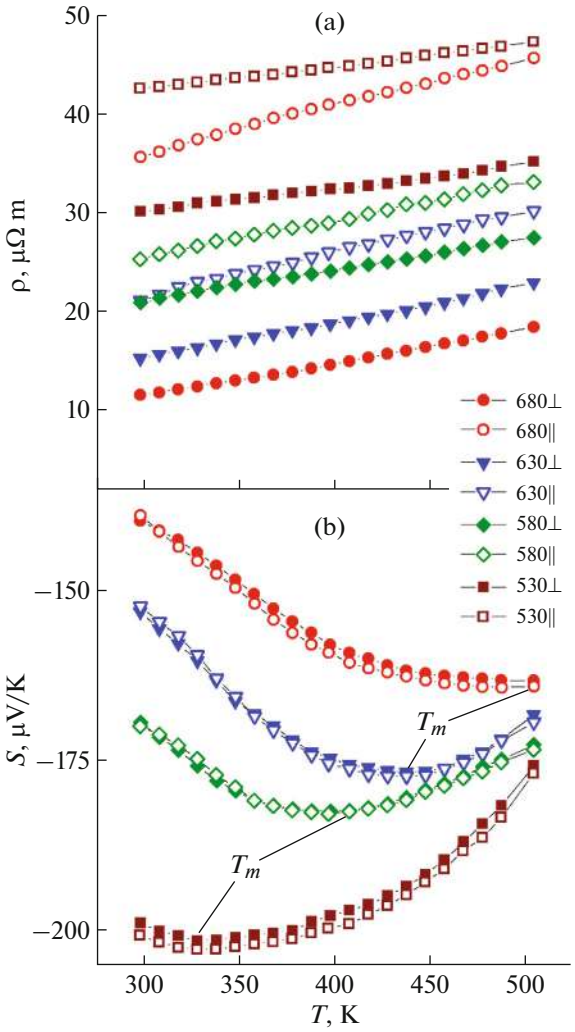

Fig. 7. Dependences ρ(T) (a) and $S(T)$ (b) for bulk materials.

$$S = \frac{2k_B^2 T m^*}{3e\hbar^2}\left(\frac{\pi}{3n}\right)^{2/3}\left(\frac{3}{2} + \gamma\right), \quad (4)$$

where k_B is Boltzmann's constant, $\hbar$ is Planck's constant, m^* is the effective mass of the electron density, and γ is the scattering coefficient.

The dependences $S(T)$ below the temperature of extrema (T_m) are T linear, which corresponds to expression (4). Above T_m, the bipolar effect becomes dominant. To implement the bipolar effect, electrons and holes must be simultaneously present in the solid. The thermal excitation of charge carriers due to their conductivity does not change the concentration of majority carriers very much, while the concentration of minority carriers will increase significantly. The

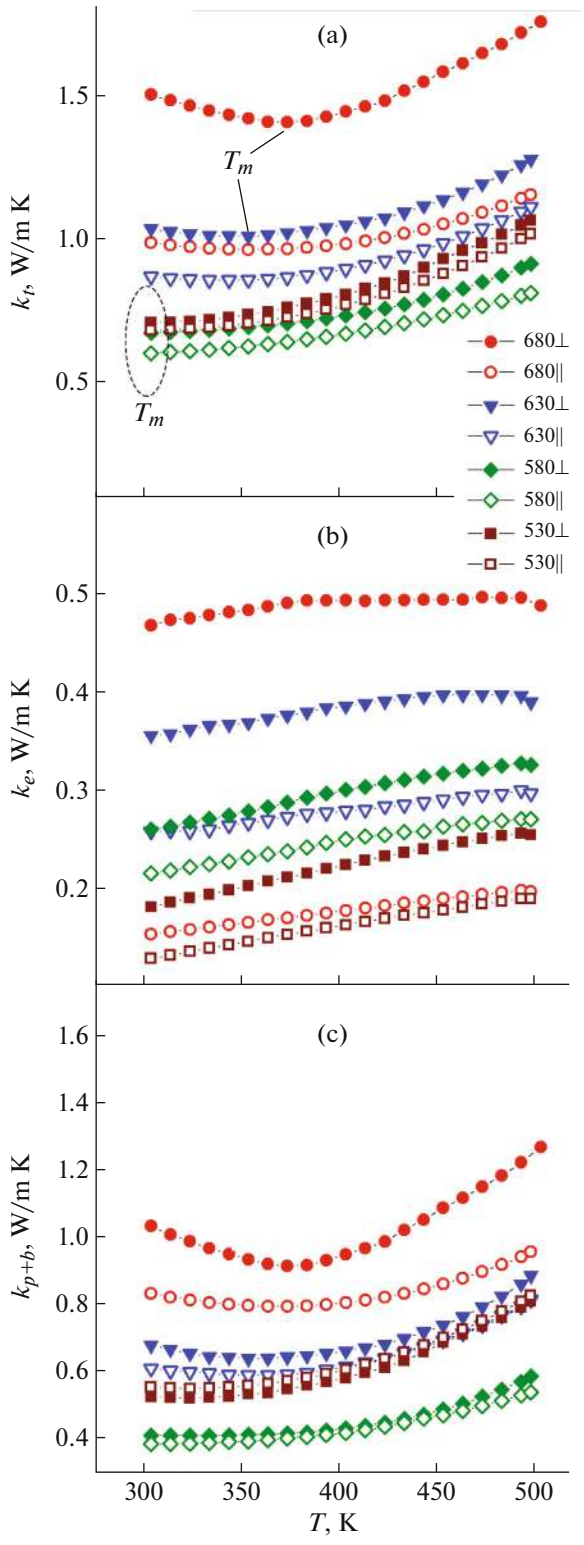

Fig. 8. Dependences $k_t(T)$ (a), $k_e(T)$ (b), and $k_{p+B}(T)$ (c) for bulk materials.

sign of the Seebeck coefficient for electronic conductivity is negative, and for hole conductivity, it is positive. The competition of two types of charge carriers leads to the formation of maxima in the $S(T)$ dependences. It was shown in [71] that the ratio of the concentration of minority (n_{min}) charge carriers to that of majority (n_{maj}) charge carriers determines the magnitude of the bipolar contribution to the thermoelectric properties. An increase in the sintering temperature leads to an increase in the concentration of the majority charge carriers and, consequently, a decrease in the value of n_{min}/n_{maj}, which generally leads to a decrease in the bipolar contribution to the Seebeck coefficient and a shift of T_m to a higher temperature region.

The $k_t(T)$ dependences taken for bulk $Bi_2Te_{2.7}Se_{0.3}$ samples based on 1D particles obtained by the SPS method at different temperatures for perpendicular and parallel measurement orientations are shown in Fig. 8a. For both sample types, the overall thermal conductivity is higher for the perpendicular ($k_{t\perp}$) measurement orientation compared to that for the parallel ($k_{t\parallel}$) orientation. Anisotropy in k_t (A_k), which is expressed by the ratio $k_{t\perp}/k_{t\parallel}$, decreases with decreasing SPS temperature ($A_k^{680} = 1.5$, $A_k^{630} = 1.2$, $A_k^{580} = 1.2$, $A_k^{530} = 1.1$; the superscripts correspond to the sintering temperature). For the test samples, the anisotropy in k_t may be due to the anisotropic effect of the grain size and changes in the degree of texturing. All $k_t(T)$ curves have a minimum at T_m, which is typical for compounds based on Bi_2Te_3 [72–75].

Typically, the total thermal conductivity includes phonon thermal conductivity k_p, electronic thermal conductivity k_e, and bipolar thermal conductivity k_B. It is known that the contribution of k_e is related to the electrical conductivity ($\sigma = 1/\rho$) by the Wiedemann–Franz law [76]:

$$k_e = L\sigma T, \tag{5}$$

where L is the Lorentz number.

In accordance with the approach proposed in [77], L and the maximum value of the Seebeck coefficient ($|S|_{max}$) are related as

$$L[10^{-8}] = 1.5 + \exp\left(-\frac{|S|_{max}\,[\mu V K^{-1}]}{116}\right). \tag{6}$$

Using expression (6), L was estimated as $L_{680} = 1.75$, $L_{630} = 1.72$, $L_{580} = 1.71$, $L_{530} = 1.88 \times 10^{-8}$ W Ω K^{-2} for bulk samples sintered at different temperatures. Using the value of L, the contributions of $k_e(T)$ to k_t were determined for the samples with perpendicular and parallel measurement orientations (Fig. 8b). The contributions $k_e(T)$ correlate with the dependences $\rho(T)$ presented in Fig. 7a.

Then the sums of the contributions of the lattice and bipolar thermal conductivities were found as $k_{p+B}(T) = k_t(T) - k_e(T)$ (Fig. 8c). Similar to the $k_t(T)$ dependences, these total contributions have minima at

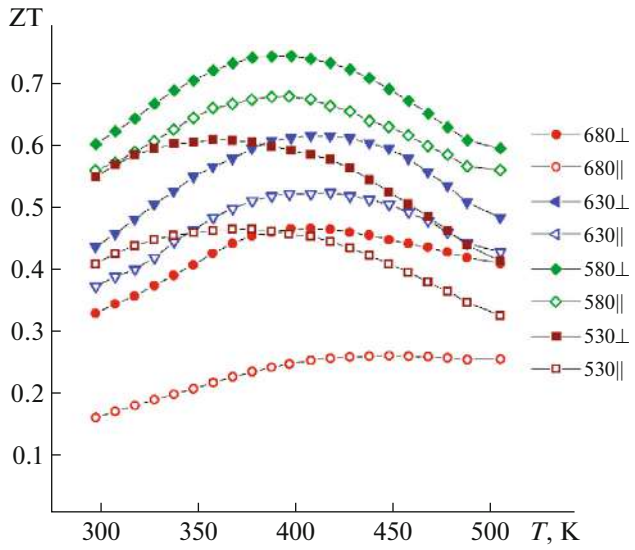

Fig. 9. Dependences ZT(T) for bulk materials $Bi_2Te_{2.7}Se_{0.3}$.

T_m. Below T_m, thermal conductivity is caused by that of the lattice. It is known that above the Debye temperature, the thermal conductivity of the lattice decreases with increasing T, obeying the law T^{-1} [60]. According to the Dulong–Petit law, the heat capacity is T independent. With increasing T, the phonon energy and the number of phonons increase linearly. The amount of phonon scattering is proportional to this number. As a result, k_p also decreases with increasing T. This mechanism is responsible for the $k_p(T) + k_B(T)$ behavior observed below T_m.

For all dependences $k_{p+B}(T)$ at room temperature, there is no contribution from k_B, and the values of k_{p+B} are determined exclusively by the phonon contribution of the thermal conductivity. Let us consider the anisotropy k_p. Anisotropy k_p (A_{kp}), expressed as $k_{p\perp}/k_{p\parallel}$, decreases with decreasing SPS temperature ($A_{kp}^{680} = 1.24$, $A_{kp}^{630} = 1.11$, $A_{kp}^{580} = 1.09$, $A_{kp}^{530} = 0.94$; the superscripts correspond to the sintering temperature), i.e., as the sintering temperature decreases, the anisotropy coefficient decreases and for the sample sintered at $T_S = 530$ K, it becomes less than unity ($k_{p\perp} < k_{p\parallel}$). Inversion of the crystallographic texture axis with decreasing SPS temperature leads to inversion of the anisotropy coefficient of the phonon contribution to thermal conductivity. This result demonstrates the potential for partial resolution of the functional thermoelectric properties (ρ, k_p).

The values of ρ, S, and k_t were used to construct the ZT(T) dependences (Fig. 9). All dependences are bell shaped. The highest ZT ≈ 0.75 (at ~400 K) was observed for the sample sintered at 580 K and measured in the direction perpendicular to the pressing direction. In general, the results of ZT calculations are in natural agreement with the results of measurements of ρ, S, and k_t. When the sintering temperature decreases from 680 to 580 K, a decrease in the anisotropy ZT is observed, and a further decrease in the sintering temperature to 530 K leads to an increase in anisotropy. The maximum value of ZT is due to the optimal ratio of ρ, S, and k_t.

CONCLUSIONS

$Bi_2Te_{2.7}Se_{0.3}$ bulk materials based on 1D particles were obtained by spark plasma sintering at different temperatures and the following conclusions were made:

(i) modified solvothermal synthesis makes it possible to obtain 1D particles based on bismuth telluride with an atypical direction of particle growth;

(ii) a decrease in the sintering temperature leads to a decrease in the average grain size, density, and a change in the degree of texturing and the direction of the crystallographic texture, which is confirmed by the XPA, SEM, and EBSD methods;

(iii) a change in the sintering temperature is responsible for a change in the chemical composition of the resulting materials (evaporation of tellurium);

(iv) the dynamics of the structural features of the morphology and tellurium concentration depending on the sintering temperature in the complex determines the change in the thermoelectric properties of the resulting materials;

(v) inversion of the direction of the axis of the crystallographic texture with a decrease in the temperature of spark plasma sintering leads to crossover of the anisotropy of the contribution of the phonon thermal conductivity.

FUNDING

The work was carried out with financial support of the Russian Science Foundation (grant no. 21-73-00199) using equipment of the Center for Collective Use of Scientific Equipment “Technologies and Materials” of the Federal State Autonomous Educational Institution of Higher Education “Belgorod National Research University.”

CONFLICT OF INTEREST

The authors of this work declare that they have no conflicts of interest.

REFERENCES

1. Y. He, T. Day, T. Zhang, et al., J. Adv. Mater. **26**, 3974 (2014).
https://doi.org/10.1002/adma.201400515

2. W. D. Liu, X. L. Shi, Z. J. Lin, et al., Appl. Energy Mater. **3**, 2192 (2020). https://doi.org/10.1021/acsaem.0c00068
3. *Handbook. Thermoelectrics. Macro to Nano*, Ed. by D. M. Rowe (CRC Taylor and Francis, Boca Raton, 2006).
4. T. Fang, X. Li, C. Hu, et al., Adv. Funct. Mater. **29**, 1900677 (2019). https://doi.org/10.1002/adfm.201900677
5. J. Xin, Y. Tang, Y. Liu, et al., Quant. Mater. **3**, 9 (2018). https://doi.org/10.1038/s41535-018-0083-6
6. A. Banik, T. Ghosh, R. Arora, et al., Energy Environ. Sci. **12**, 589 (2019). https://doi.org/10.1039/C8EE03162B
7. K. Biswas, J. He, G. Wang, et al., Energy Environ. Sci. **4**, 4675 (2011). https://doi.org/10.1039/C1EE02297K
8. J. H. Chu, M. Gu, T. Zhu, et al., Energy Environ. Sci. **12**, 3390 (2019). https://doi.org/10.1039/C9EE02228G
9. P. F. Qiu, T. Mao, Z. F. Huang, et al., Joule **3**, 1538 (2019). https://doi.org/10.1016/j.joule.2019.04.010
10. J. Yang, L. Xi, W. Qiu, et al., npj Comput. Mater. **2**, 15015 (2016). https://doi.org/10.1038/npjcompumats.2015.15
11. B. Qin, D. Wang, W. He, et al., J. Am. Chem. Soc. **141**, 1141 (2019). https://doi.org/10.1021/jacs.8b12450
12. C. Chang, D. Y. Wang, D.S. He, et al., Adv. Energy Mater. **9**, 1901334 (2019). https://doi.org/10.1002/aenm.201901334
13. C. Chang, M. Wu, D. He, et al., Science **360**, 778 (2018). https://doi.org/10.1126/science.aaq1479
14. L. D. Zhao, G. Tan, S. Hao, et al., Science **351**, 141 (2016). https://doi.org/10.1126/science.aad3749
15. L. D. Zhao, J. He, D. Berardan, et al., Energy Environ. Sci. **7**, 2900 (2014). https://doi.org/10.1039/C4EE00997E
16. L. D. Zhao, S. H. Lo, Y. S. Zhang, et al., Nature **508**, 373 (2014). https://doi.org/10.1038/nature13184
17. Y. Hosokawa, T, Koji, and T. Masayuki, Sci. Rep. **9**, 10790 (2019). https://doi.org/10.1038/s41598-019-47356-5
18. H. Kaibe, Y. Tanaka, M. Sakata, and I. J. Nishida, Phys. Chem. Solids **50**, 945 (1989). https://doi.org/10.1016/0022-3697(89)90045-0
19. K. Yamauchi and M. Takashiri, J. Alloys Compd. **698**, 977 (2017). https://doi.org/10.1016/j.jallcom.2016.12.284
20. S. Kudo, S. Tanaka, K. Miyazaki, et al., Mater. Trans. **58**, 513 (2017). https://doi.org/10.2320/matertrans.M2016295
21. G. Han, Z. G. Chen, L. Yang, et al., ACS Appl. Mater. Interfaces **7**, 989 (2015). https://doi.org/10.1021/am5078528
22. M. Yaprintsev, A. Vasil'ev, O. Ivanov, et al., Solid State Sci. **135**, 107083 (2023). https://doi.org/10.1016/j.solidstatesciences.2022.107083
23. R.J. Mehta, Y. L. Zhang, C. Karthik, et al., Nat. Mater. **11**, 233 (2012). https://doi.org/10.1038/nmat3213
24. A. Soni, Y. Y. Zhao, L. G. Yu, et al., Nano Lett. **12**, 1203 (2012). https://doi.org/10.1021/nl2034859
25. M. Scheele, N. Oeschler, I. Veremchuk, et al., ACS Nano **4**, 4283 (2010). https://doi.org/10.1021/nn1008963
26. Y. Min, J. W. Roh, H. Yang, et al., Adv. Mater. **25**, 1425 (2013). https://doi.org/10.1002/adma.201203764
27. Y. Zhang, L.P. Hu, T. J. Zhu, et al., Cryst. Growth Des. **13**, 645 (2013). https://doi.org/10.1021/cg3013156
28. J.P. Fu, S. Y. Song, X. G. Zhang, et al., CrystEngComm **14**, 2159 (2012). https://doi.org/10.1039/C2CE06348D
29. G. Zhang, B. Kirk, L.A. Jauregui, et al., Nano Lett. **12**, 56 (2011). https://doi.org/10.1021/nl202935k
30. J. S. Son, M. K. Choi, M. K. Han, et al., Nano Lett. **12**, 640 (2012). https://doi.org/10.1021/nl203389x
31. G. Zhang, H. Fang, H. Yang, et al., Nano Lett. **12**, 3627 (2012). https://doi.org/10.1021/nl301327d
32. L. Cheng, Z. G. Chen, L. Yang et al., J. Phys. Chem. C **117**, 12458 (2013). https://doi.org/10.1021/jp4041666
33. R.J. Mehta, C. Karthik, B. Singh, et al., ACS Nano **4**, 5055 (2010). https://doi.org/10.1021/nn101322p
34. Y. C. Zhang, H. Wang, S. Kraemer, et al., ACS Nano **5**, 3158 (2011). https://doi.org/10.1021/nn2002294
35. S. Y. Song, J. Fu, X. Y. Li, et al., Chem. Eur. J. **19**, 2889 (2013). https://doi.org/10.1002/chem.201203437
36. Z. Chai, H. Wang, Q. Suo, et al., CrystEngComm **16**, 3507 (2014). https://doi.org/10.1039/C4CE00005F
37. H. T. Zhu, J. Luo, and J. K. Liang, J. Mater. Chem. A **2**, 12821 (2014). https://doi.org/10.1039/C4TA02532F
38. L. D. Hicks and M.S. Dresselhaus, Phys. Rev. B **47**, 16631 (1993). https://doi.org/10.1103/PhysRevB.47.16631
39. A. I. Hochbaum, R. K. Chen, R. D. Delgado, et al., Nature **451**, 163 (2008). https://doi.org/10.1038/nature06381
40. M. Yaprintsev, O. Ivanov, and A. Vasil'ev, J. Solid State Chem. **308**, 122945 (2022). https://doi.org/10.1016/j.jssc.2022.122945
41. M. Yaprintsev, A. Vasil'ev, and O. Ivanov, J. Alloys Compd. **900**, 163516 (2022). https://doi.org/10.1016/j.jallcom.2021.163516

42. M. Yaprintsev, A. Vasil'ev, O. Ivanov, et al., J. Solid State Chem. **312**, 123176 (2022). https://doi.org/10.1016/j.jssc.2022.123176
43. M. Yaprintsev, O. Ivanov, A. Vasil'ev, et al., J. Solid State Chem. **297**, 122047 (2021). https://doi.org/10.1016/j.jssc.2021.122047
44. O. Ivanov, M. Yaprintsev, and A. Vasil'ev, J. Eur. Ceram. Soc. **40**, 3431 (2020). https://doi.org/10.1016/j.jeurceramsoc.2020.03.048
45. O. Ivanov, M. Yaprintsev, and A. Vasil'ev, J. Solid State Chem. **290**, 121559 (2020). https://doi.org/10.1016/j.jssc.2020.121559
46. M. Yaprintsev, A. Vasil'ev, and O. Ivanov, J. Eur. Ceram. Soc. **40**, 742 (2020). https://doi.org/10.1016/j.jeurceramsoc.2019.11.028
47. A. Vasil'ev, M. Yaprintsev, O. Ivanov, et al., Solid State Sci. **84**, 28 (2018). https://doi.org/10.1016/j.solidstatesciences.2018.08.004
48. P. Pyykkö and M. Atsumi, Chem. Eur. J. **15**, 186 (2009). https://doi.org/10.1002/chem.200800987
49. X. Yan, B. Poudel, Y. Ma, et al., Nano Lett. **10**, 3373 (2010). https://doi.org/10.1021/nl101156v
50. M. S. Dresselhaus, Y. Ligen, A. Soni, et al., Nano Lett. **12**, 1203 (2012). https://doi.org/10.1021/nl2034859
51. Q. Li, Z. Wei, Q. Ma, et al., ACS Omega **6**, 33883 (2021). https://doi.org/10.1021/acsomega.1c05160
52. F. K. Lotgering, J. Inorg. Nucl. Chem. **9**, 113 (1959). https://doi.org/10.1016/0022-1902(59)80070-1
53. Y. Liu, Y. Zhang, K. H. Lim, et al., ACS Nano **12**, 7174 (2018). https://doi.org/10.1021/acsnano.8b03099
54. X. A. Fan, J. Y. Yang, R. G. Chen, et al., J. Phys. D: Appl. Phys. **39**, 740 (2006). https://doi.org/10.1088/0022-3727/39/4/021
55. J. Jiang, L. Chen, S. Bai, et al., Mater. Sci. Eng. B **117**, 334 (2005). https://doi.org/10.1016/j.mseb.2005.01.002
56. Q. Lognon, F. Gascoin, O. I. Lebedev, et al., J. Am. Ceram. Soc. **97**, 2038 (2014). https://doi.org/10.1111/jace.12970
57. O. Ivanov, M. Yaprintsev, A. Vasil'ev, et al., J. Alloys Compd. **872**, 159743 (2021). https://doi.org/10.1016/j.jallcom.2021.159743
58. J. R. Drabble and C. H. L. Goodman, J. Phys. Chem. Solid. **5**, 142 (1958). https://doi.org/10.1016/0022-3697(58)90139-2
59. S. Nakajima, J. Phys. Chem. Solid. **24**, 479 (1963). https://doi.org/10.1016/0022-3697(63)90207-5
60. J. Blakemore and J. Sydney, *Solid State Physics* (Cambridge Univ. Press, 1985).
61. M. Yaprintsev, R. Lyubushkin, O. Soklakova, and O. Ivanov, J. Electron. Mater. **47**, 1362 (2018). https://doi.org/10.1007/s11664-017-5940-8
62. Y. Pan, T. R. Wei, C. F. Wu, et al., Mater. Chem. C **3**, 10583 (2015). https://doi.org/10.1039/C5TC02219C
63. L. Hu, T. Zhu, X. Liu, and X. Zhao, Adv. Funct. Mater. **4**, 5211 (2014). https://doi.org/10.1002/adfm.201400474
64. J. Suh, K. M. Yu, D. Fu, et al., Adv. Mater. **27**, 3681 (2015). https://doi.org/10.1002/adma.201501350
65. B. S. A. Humphry and C. A. Schuh, Nano Energy **36**, 223 (2017). https://doi.org/10.1016/j.nanoen.2017.04.018
66. J. Lee, J. Kim, W. Moon, et al., J. Phys. Chem. C **116**, 19512 (2012). https://doi.org/10.1021/jp3030039
67. J. Lee, A. Berger, L. U. Cagnon, et al., Phys. Chem. Chem. Phys. **12**, 15247 (2010). https://doi.org/10.1039/C0CP00749H
68. N. T. Nghi, A. L. Usiikans, and T. A. Cherepanova, Cryst. Res. Technol. **21**, 367 (1986). https://doi.org/10.1002/crat.2170210309
69. C.V. Manzano, B. Abad, M. Muñoz Rojo, et al., Sci. Rep. **6**, 19129 (2016). https://doi.org/10.1038/srep19129
70. K. C. Lukas, W. C. Liu, Z. F. Ren, and C. P. Opeil, J. Appl. Phys. **112**, 054509 (2012). https://doi.org/10.1063/1.4749806
71. H. S. K im, K. H. Lee, and S. Kim, J. Mater. Res. Technol. **14**, 639 (2021). https://doi.org/10.1016/j.jmrt.2021.06.087
72. M. Yapryntsev, A. Vasil'ev, and O. Ivanov, J. Eur. Ceram. Soc. **39**, 1193 (2019). https://doi.org/10.1016/j.jeurceramsoc.2018.12.041
73. J. Yang, F. Wu, Z. Zhu, et al., J. Alloys Compd. **619**, 401 (2015). https://doi.org/10.1016/j.jallcom.2014.09.024
74. X. H. Ji, X. B. Zhao, Y. H. Zhang, et al., J. Alloys Compd. **387**, 282 (2005). https://doi.org/10.1016/j.jallcom.2004.06.047
75. F. Wu, H. Song, J. Jia, and X. Hu, Prog. Nat. Sci. Mater. Int. **23**, 408 (2013). https://doi.org/10.1016/j.pnsc.2013.06.007
76. W. Liu, X. Yan, G. Chen, and Z. Ren, Nano Energy **1**, 42 (2012). https://doi.org/10.1016/j.nanoen.2011.10.001
77. H. Kim, Z. Gibbs, Y. Tang, et al., Apl. Mater. **3**, 041506 (2013). https://doi.org/10.1063/1.4908244

Translated by Sh. Galyaltdinov